
Chapter 2: Changes in Atmospheric Constituents and in Radiative Forcing

Figures

Coordinating Lead Authors: Piers Forster (UK), V. Ramaswamy (USA)

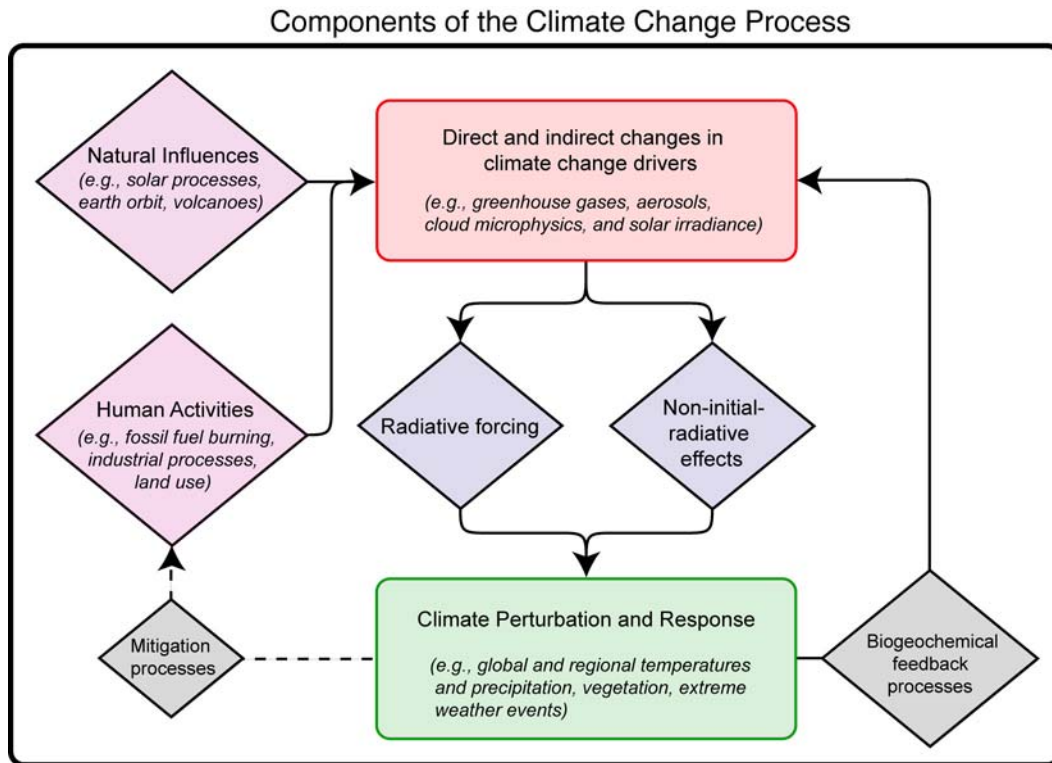
Lead Authors: Paulo Artaxo (Brasil), Terje Berntsen (Norway), Richard A. Betts (UK), David W. Fahey (USA), James Haywood (UK), Judith Lean (USA), David C. Lowe (New Zealand), Gunnar Myhre (Norway), John Nganga (Kenya), Ronald Prinn (USA, New Zealand), Graciela Raga (Mexico, Argentina), Michael Schulz (France, Germany), Robert Van Dorland (Netherlands)

Contributing Authors: Greg Bodeker (New Zealand), Olivier Boucher (UK, France), William Collins (USA), Thomas J. Conway (USA), Ed Dlugokencky (USA), James W. Elkins (USA), David Etheridge (Australia), Peter Foukal (USA), Paul Fraser (Australia), Marvin Geller (USA), Fortunat Joos (Switzerland), C. David Keeling (USA), Ralph Keeling (USA), Stefan Kinne (Germany), Keith Lassey (New Zealand), Ulrike Lohmann (Switzerland), Andrew Manning (UK, New Zealand), Steve Montzka (USA), David Oram (UK), Kath O'Shaughnessy (New Zealand), Stephen Piper (USA), Gian-Kasper Plattner (Switzerland), Michael Ponater (Germany), Navin Ramankutty (USA, India), George Reid (USA), David Rind (USA), Karen Rosenlof (USA), Robert Sausen (Germany), Dan Schwarzkopf (USA), S. Solanki (Germany), Georgiy Stenchikov (USA), Nicola Stuber (UK, Germany), Toshihiko Takemura (Japan), Christiane Textor (France, Germany), Ray Wang (USA), Ray Weiss (USA), Tim Whorf (USA)

Review Editors: Teruyuki Nakajima (Japan), V. Ramanathan (USA)

Date of Draft: 27 October 2006

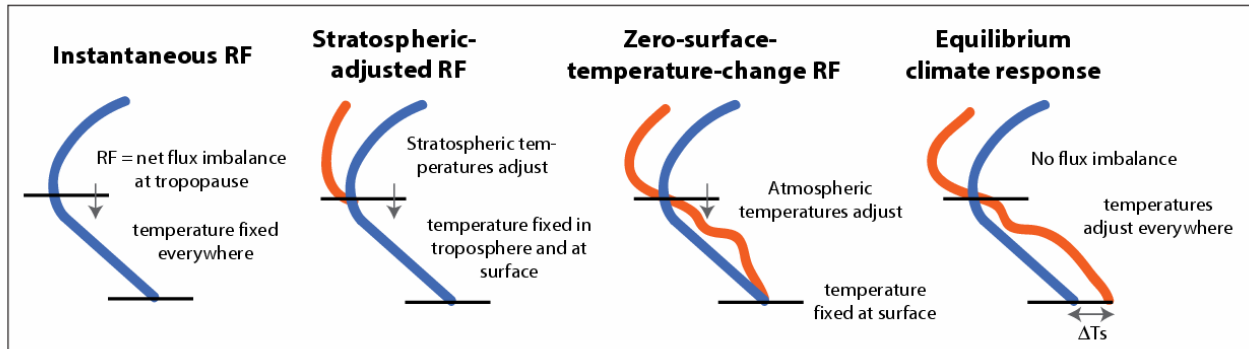
1
2



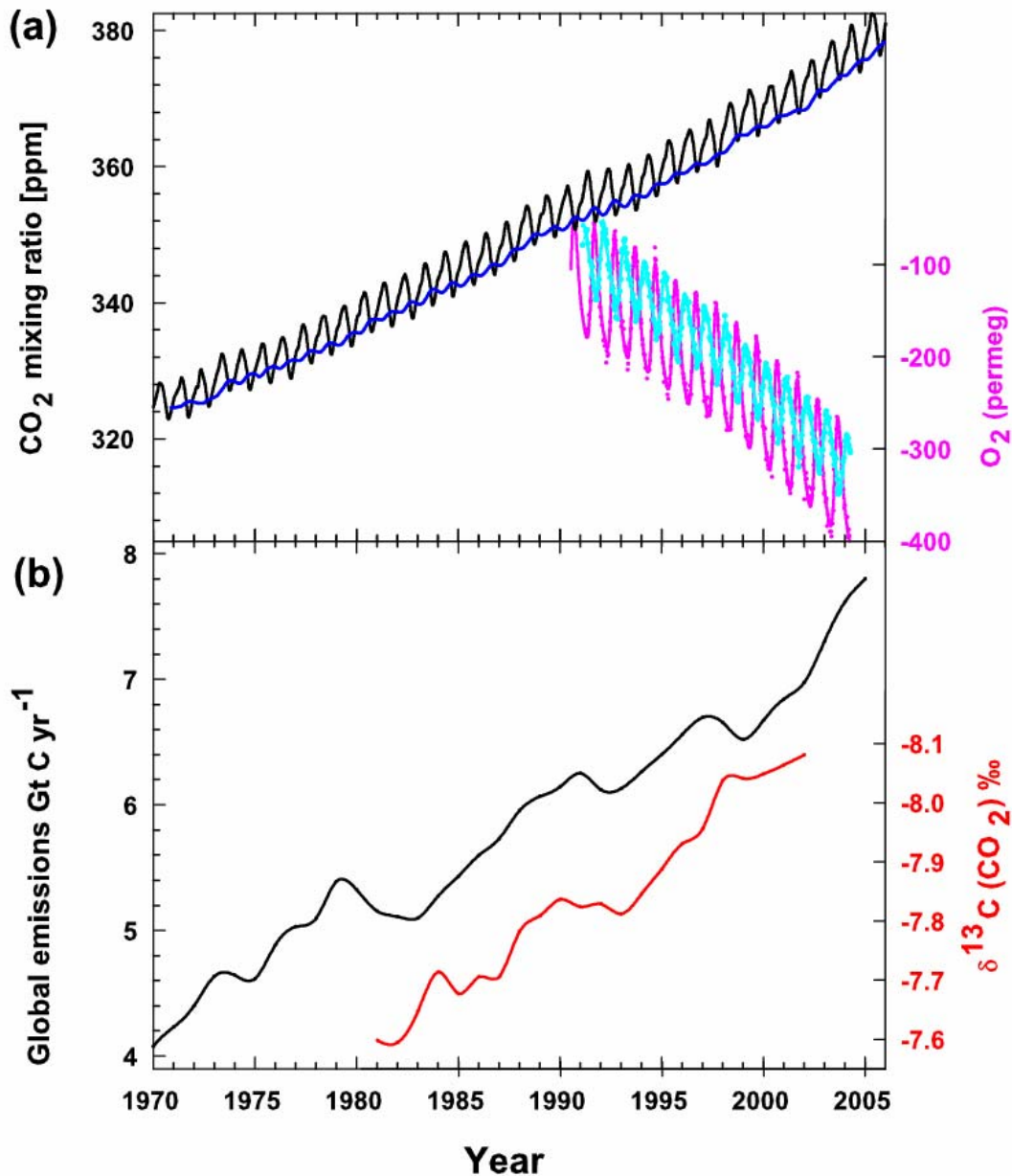
3
4
5
6
7
8
9
10
11
12
13

Figure 2.1. Diagram illustrating how RF is linked to other aspects of climate change being assessed by the IPCC. Human activities and natural processes cause direct and indirect changes in climate change drivers. In general, these changes result in specific RF changes, either positive or negative, and cause some non-initial-radiative effects, such as changes in evaporation. RF and non-initial-radiative effects lead to climate perturbations and responses as discussed in Chapters 6-8. Attribution of climate change to natural and anthropogenic factors is discussed in Chapter 9. The coupling amongst biogeochemical processes leads to feedbacks from climate change to its drivers (Chapter 7). An example of feedbacks is changes in wetland emissions of methane that may occur in a warmer climate. The potential approaches to mitigating climate change by altering human activities (dashed lines) is a topic of Working Group III.

1
2



3
4 **Figure 2.2.** Schematic comparing RF calculation methodologies. RF, defined as the net flux imbalance at the
5 tropopause, is shown by an arrow. The horizontal lines represent the surface (lower line) and tropopause
6 (upper line). The unperturbed temperature profile is shown as the blue line and the perturbed temperature
7 profile as the red line. From left to right: Instantaneous RF: atmospheric temperatures are fixed everywhere;
8 Stratospheric-adjusted RF: allows stratospheric temperatures to adjust; Zero-surface-temperature-change RF:
9 allows atmospheric temperatures to adjust everywhere with surface temperatures fixed; and Equilibrium
10 climate response: allows the atmospheric and surface temperatures to adjust to reach equilibrium (no
11 tropopause flux imbalance), giving a surface-temperature change (ΔT_s).
12

1
2

3
4 **Figure 2.3.** Recent CO₂ concentrations and emissions. Panel (a) shows CO₂ concentrations (monthly
5 averages) measured by continuous analysers over the period 1970 to 2005 from Mauna Loa, Hawaii (19°N,
6 black) (Keeling and Whorf, 2005) and Baring Head, New Zealand (41°S, blue) (following techniques by
7 Manning et al., 1997). Due to the larger amount of terrestrial biosphere in the Northern hemisphere, seasonal
8 cycles in CO₂ are larger there than in the Southern hemisphere. In the lower right of the panel, atmospheric
9 oxygen measurements from flask samples are shown from Alert, Canada (82°N, pink) and Cape Grim,
10 Australia (41°S, cyan) (Manning and Keeling, 2006). The O₂ concentration is measured as “per meg”
11 deviations in the O₂/N₂ ratio from an arbitrary reference, analogous to the “per mil” unit typically used in
12 stable isotope work, but where the ratio is multiplied by 10⁶ instead of 10³ because much smaller changes are
13 measured. Panel (b) shows the annual global CO₂ emissions from fossil-fuel burning and cement
14 manufacture in GtC yr⁻¹ (black) through to 2005, using data from the CDIAC website (Marland et al, 2006)
15 to 2003. Emissions data for 2004 and 2005 are extrapolated from CDIAC using data from the BP Statistical
16 Review of World Energy 2006. Land-use emissions are not shown, these are estimated to be between 0.5–2.7
17 GtC yr⁻¹ for the 1990s (Chapter 7, Table 7.2). Annual averages of the ¹³C/¹²C ratio measured in atmospheric
18 CO₂ at Mauna Loa from 1981 to 2002 (red) are also shown (Keeling et al, 2005). The isotope data are

1 expressed as $\delta^{13}\text{C}(\text{CO}_2)$ “‰” (per mil) deviation from a calibration standard. Note that this scale is inverted
2 to improve clarity.
3

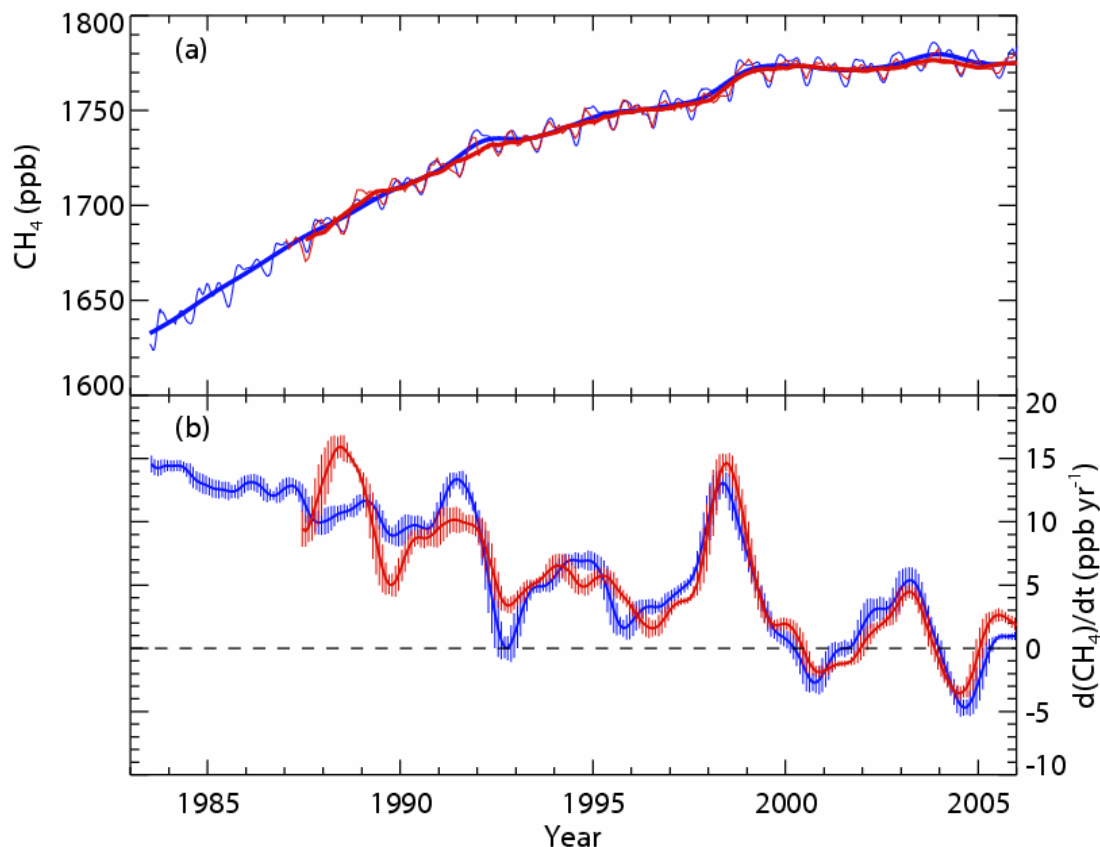
1
23
4
5
6
7
8
9
10
11
12
13
14
15
16
17

Figure 2.4. Recent methane concentrations and trends. (a) Time series of global methane abundance mole fraction (in ppb) derived from surface sites operated by NOAA/GMD (blue lines) and AGAGE (red lines). The thinner lines show the methane global averages and the thicker lines are the deseasonalized global average trends from both networks (b) Annual growth rate (ppb yr⁻¹) in global atmospheric methane abundance from 1984 through to the end of 2005 (NOAA/GMD blue), and 1988 to the end of 2005 (AGAGE red). To derive the growth rates and their uncertainties for each month, a linear least squares method that takes account of the auto correlation of residuals is used. This follows the methods of Wang et al. (2002) and is applied to the deseasonalized global mean mole fractions from (a), for values 6 months before and after the current month. The vertical lines indicate $\pm 2\sigma$ uncertainties (95% confidence interval), and 1σ uncertainties are between 0.1 to 1.4 ppb yr⁻¹ for both AGAGE and NOAA/GMD. Note that the differences between AGAGE and NOAA/GMD calibration scales are determined through occasional intercomparisons.

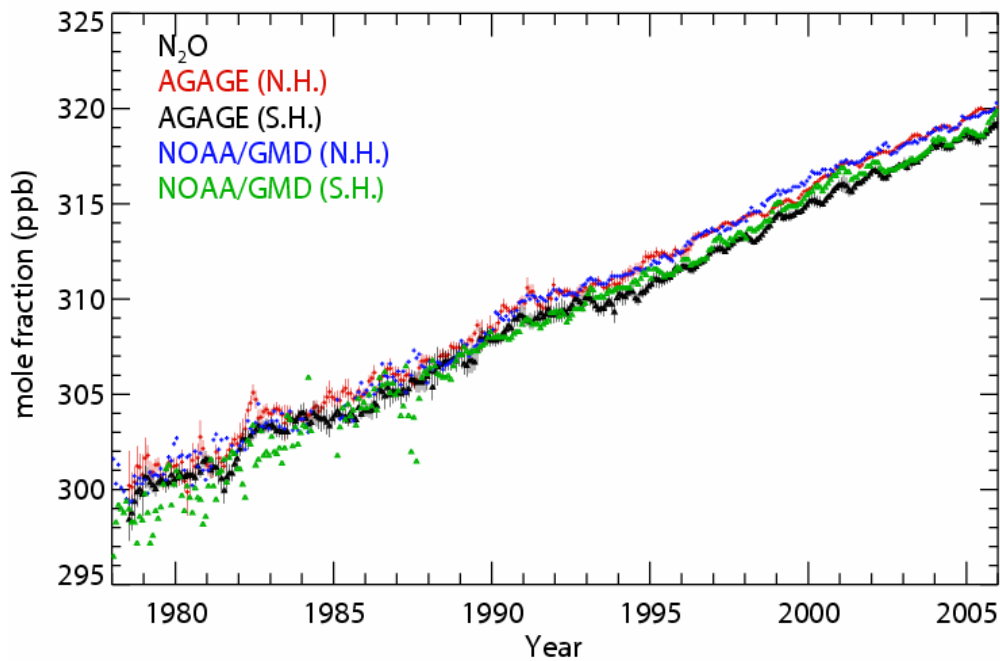
1
23
4
5
6
7
8
9
10
11

Figure 2.5. Hemispheric monthly mean N₂O mole fractions (in ppb) (crosses for Northern and triangles for Southern Hemisphere). Observations (*in-situ*) of N₂O from ALE and GAGE (through mid-1990s) and AGAGE (since mid-1990s) networks (Prinn et al., 2000; Prinn et al., 2005b) are shown with monthly standard deviations. Data from NOAA-GMD are shown without these standard deviations (Thompson et al., 2004). The general decrease in the variability of the measurements over time is due mainly to improved instrumental precision. The real signal emerges only in the last decade.

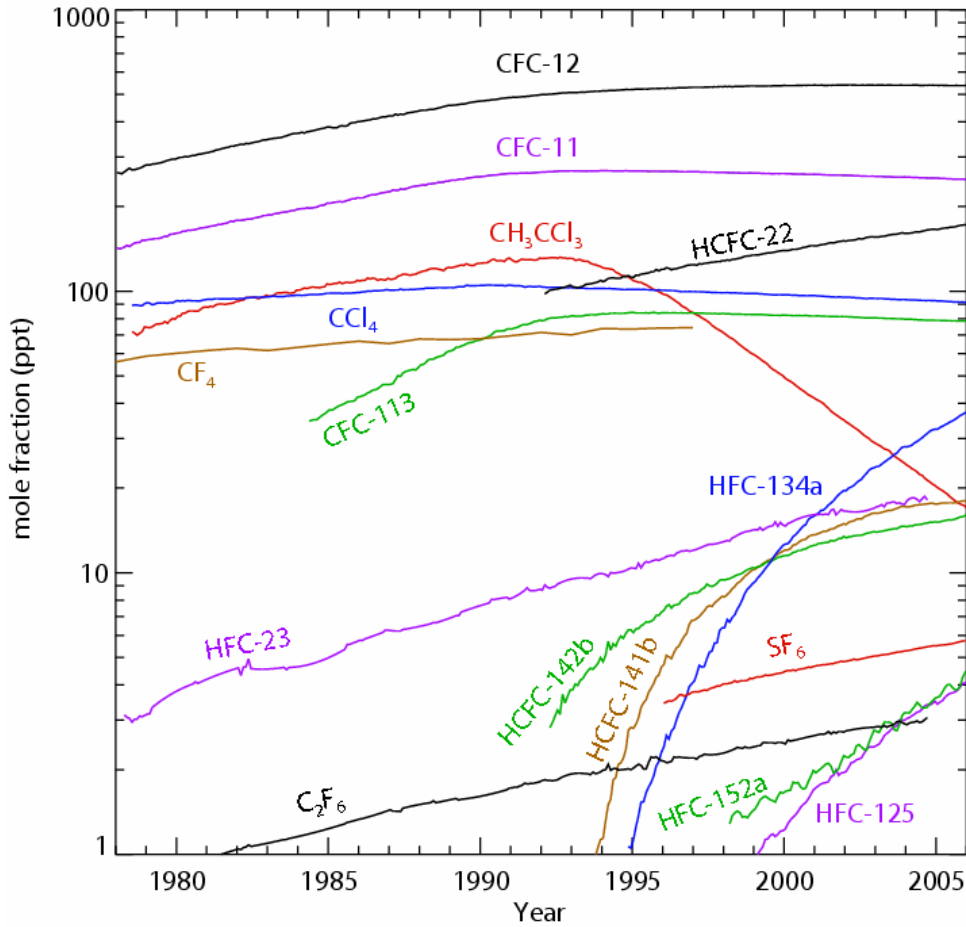
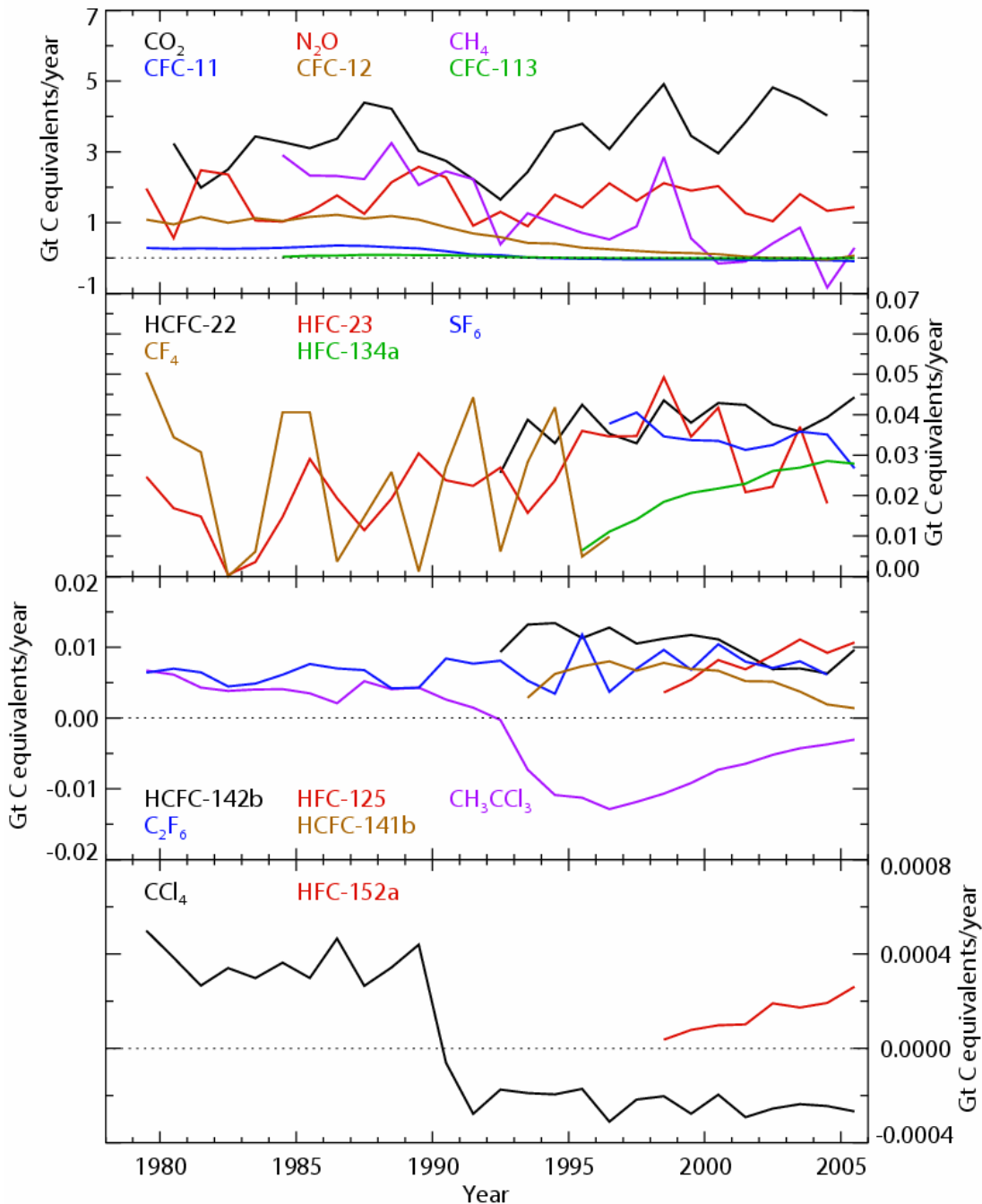
1
23
4
5
6
7
8
9
10
11

Figure 2.6. Temporal evolution of the global-average dry-air mole fractions (ppt) of the major halogen-containing LLGHGs. These are derived mainly using monthly-mean measurements from the AGAGE and NOAA-GMD networks. For clarity, the two network values are averaged with equal weight when both are available. While differences exist, these network measurements agree reasonably well with each other [except for CCl_4 (2–4%) and HCFC-142b (3–6%)], and with other measurements where available (see text for references for each gas).

1
2



3
4
5
6
7
8
9
10
11
12
13
14
15

Figure 2.7. Annual rates of change of the global atmospheric masses of each of the major LLGHGs expressed in common units of GtC year^{-1} . These rates are computed from their actual annual mass changes in Gt year^{-1} (as derived from their observed global- and annual-average mole fractions presented in Figures 2.3 to 2.6 and discussed in Sections 2.3.1 to 2.3.4) by multiplying them by their global warming potentials for 100-year time horizons and then dividing by the ratio of the CO_2 to C masses (44/12). These rates are positive/negative whenever the mole fractions are increasing/decreasing respectively. Use of these common units provides an approximate way to intercompare the fluxes of LLGHGs, using the same approach employed to intercompare the values of LLGHG emissions under the Kyoto Protocol (see e.g., Prinn, 2004). Note that the negative indirect RF of CFCs and HCFCs due to stratospheric ozone depletion is not included. The oscillations in the CF_4 curve may result partly from truncation in reported mole fractions.

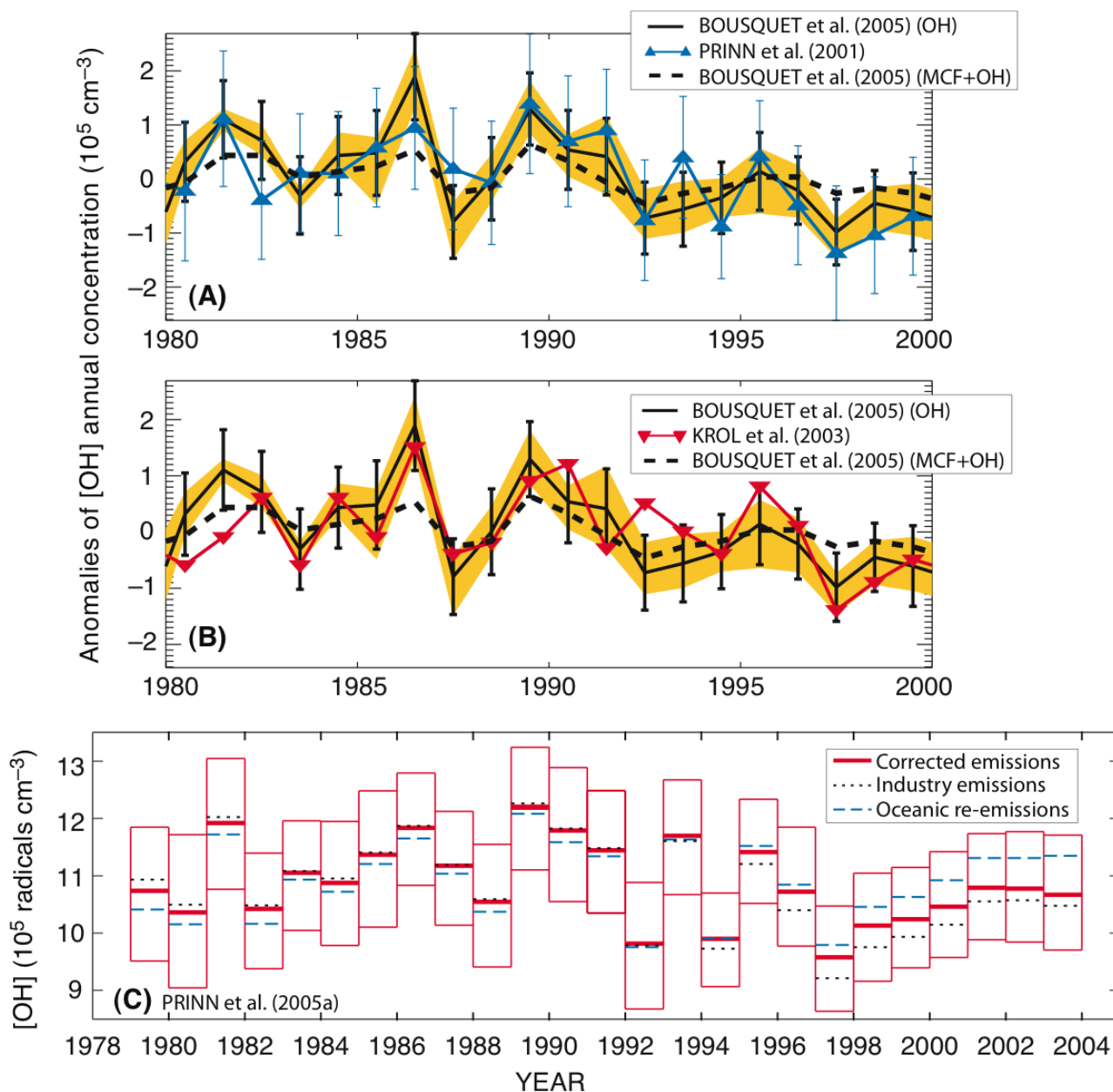
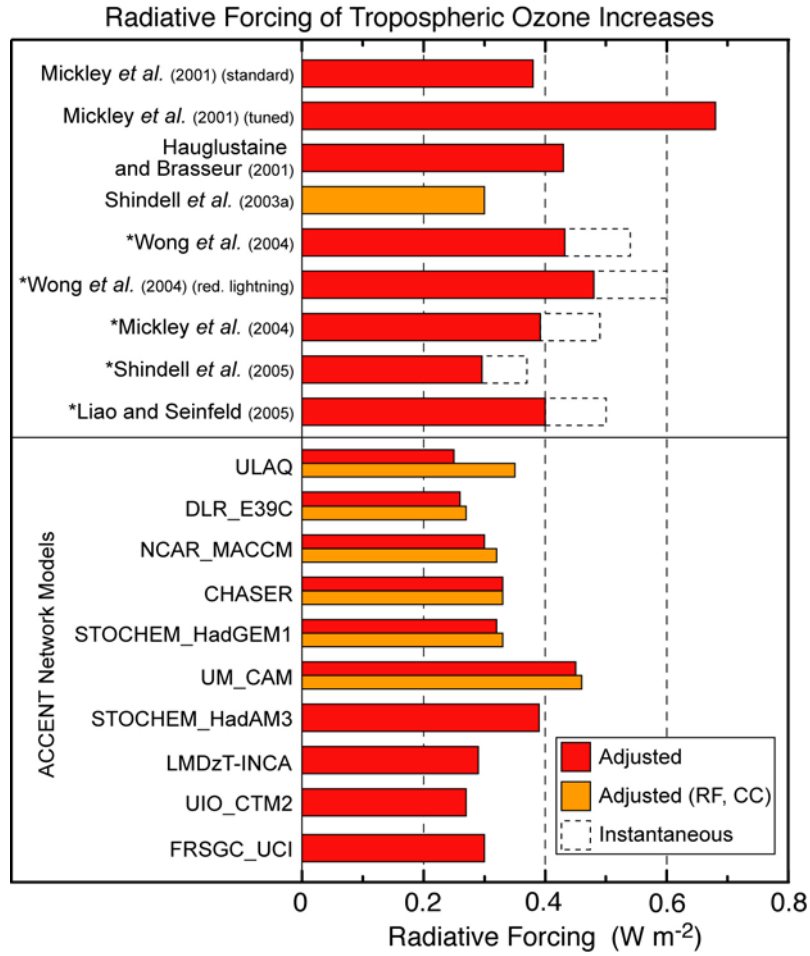
1
23
4
5
6
7
8
9
10
11
12
13
14
15

Figure 2.8. Estimates used to evaluate trends in weighted global-average OH concentrations. (A) and (B): comparison of 1980–1999 OH anomalies (relative to their long-term means) inferred by Bousquet et al. (2005), Prinn et al. (2001) and Krol et al. (2003) from AGAGE methyl chloroform (CH_3CCl_3) observations, and by Bousquet et al. (2005) when CH_3CCl_3 emissions as well as OH are inferred; error bars for Bousquet et al. (2005) refer to 1σ inversion errors while yellow areas refer to envelope of their 18 OH inversions. (C) OH concentrations for 1979–2003 inferred by Prinn et al. (2005a) (utilizing industry emissions corrected using recent CH_3CCl_3 observations), showing the recovery of 2003 OH levels to 1979 levels; also shown are results assuming uncorrected emissions and estimates of recent oceanic re-emissions. Error bars in Prinn et al. (2001, 2005a) are 1σ and include inversion, model, emission and calibration errors from large Monte Carlo ensembles (see Section 2.3.5 for details and references).

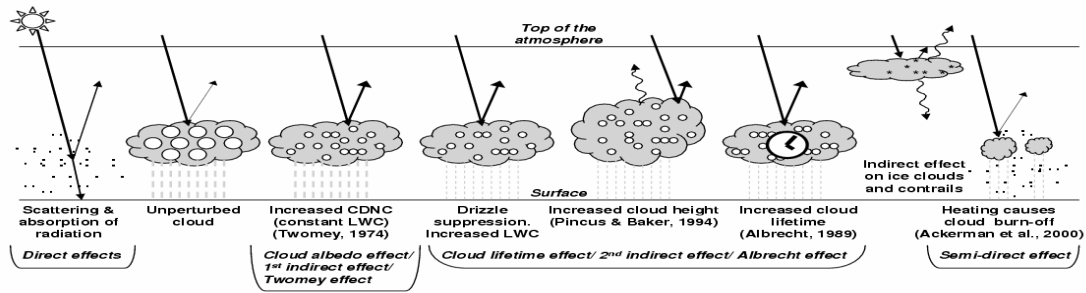
1
2



3
4
5
6
7
8
9
10
11

Figure 2.9. Calculated RF due to tropospheric ozone change since preindustrial time based on CTM and GCM model simulations published since the TAR. Estimates with GCMs including the effect of climate change since 1750 are given by orange bars (Adjusted RF, CC). Studies denoted with an (*) give only instantaneous RF in the original publications. Stratospheric-adjusted RF for these are estimated by reducing the instantaneous RF (indicated by the dashed bars) by 20%. The instantaneous RF from Mickley *et al.* (2001) is reported as an adjusted RF in Gauss *et al.* (2006).

1
2



3
4
5
6
7
8
9
10
11
12
13
14

Figure 2.10. Schematic diagram showing the various radiative mechanisms associated with cloud effects that have been identified as significant in relation to aerosols (modified from Haywood and Boucher, 2000). The small black dots represent aerosol particles, the larger open circles cloud droplets. Straight lines represent the incident and reflected solar radiation, and wavy lines represent terrestrial radiation. The filled white circles indicate cloud droplet number concentration (CDNC). The unperturbed cloud contains larger cloud drops as only natural aerosols are available as cloud condensation nuclei, while the perturbed cloud contains a greater number of smaller cloud drops as both natural and anthropogenic aerosols are available as cloud condensation nuclei (CCN). The vertical grey dashes represent rainfall. LWC refers to the liquid water content.

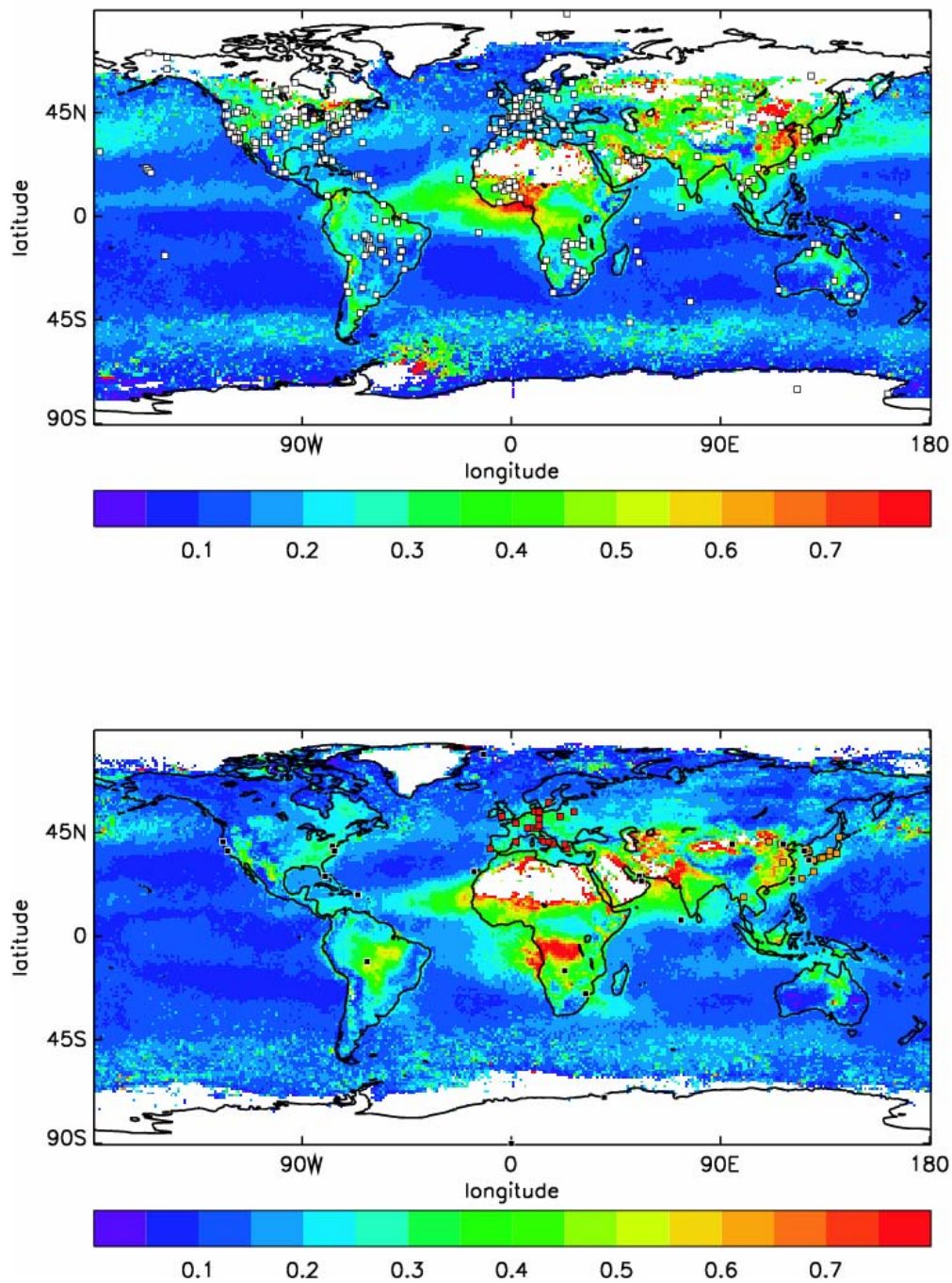
1
23
4
5
6
7
8
9
10

Figure 2.11. Aerosol optical depth, τ_{aer} , at $0.55 \mu\text{m}$ (colour bar) as determined by the MODIS instrument for the January to March 2001 mean (top panel) and for August to October 2001 mean (bottom panel). The top panel also shows the location of AERONET sites (white squares) that have been operated (not necessary continuously) since 1996. The bottom panel also shows the location of different aerosol lidar networks (red = EARLINET, orange = ADNET, black = MPLNET).

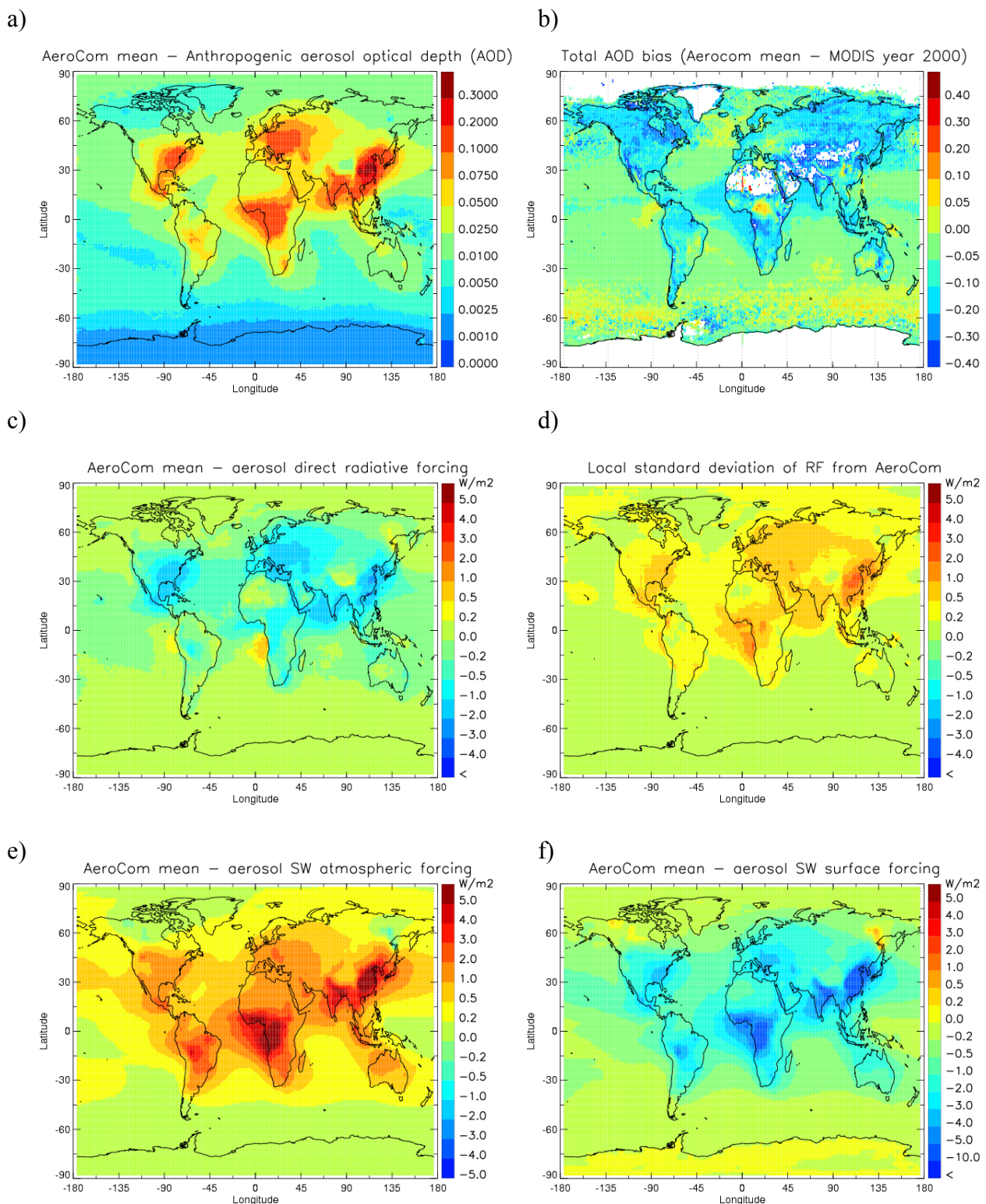
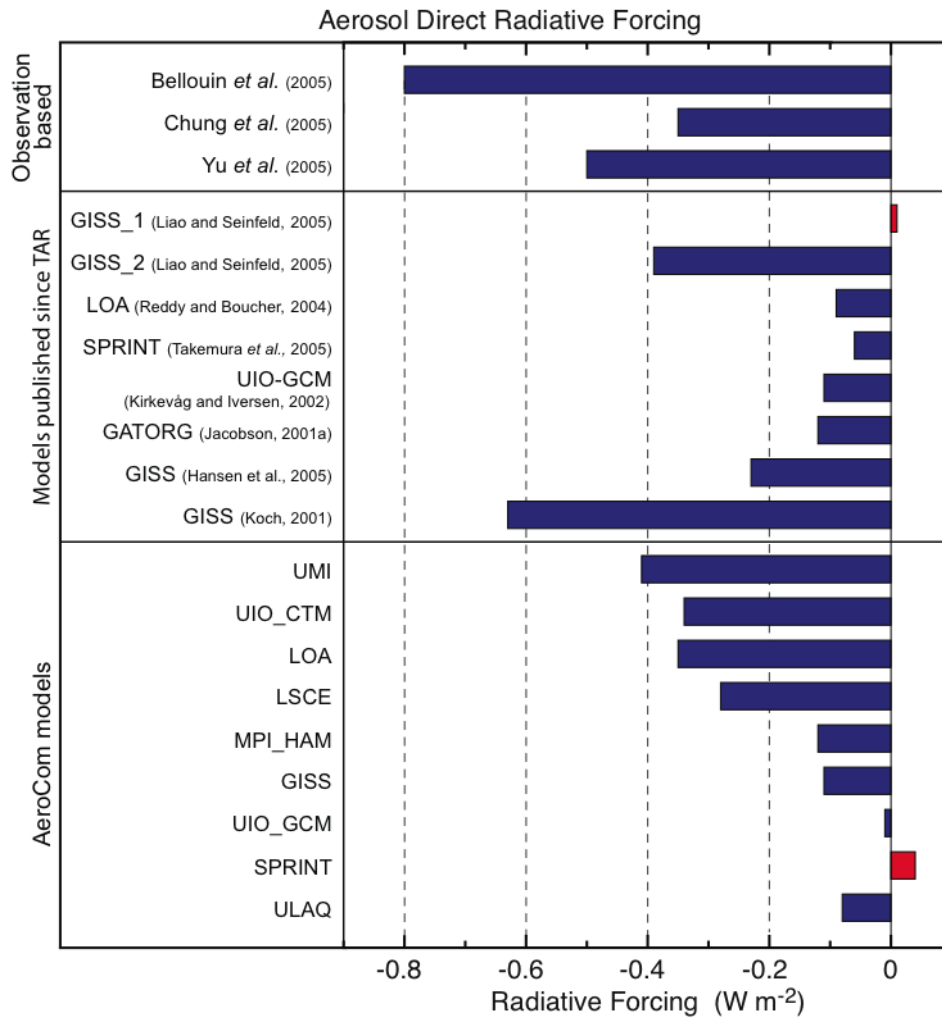


Figure 2.12. Characteristic aerosol properties related to their radiative effects, derived as the mean of the results from the 9 AeroCom models listed in Table 2.5. All panels except (b) relate to the combined anthropogenic aerosol effect. Panel (b) considers the total (natural + anthropogenic) aerosol optical depth from the models. (a) Aerosol optical depth. (b) Difference in total aerosol optical depth between model and MODIS data. (c) Shortwave RF. (d) Standard deviation of RF from the model results. (e) Shortwave forcing of the atmosphere. (f) Shortwave *surface forcing*.

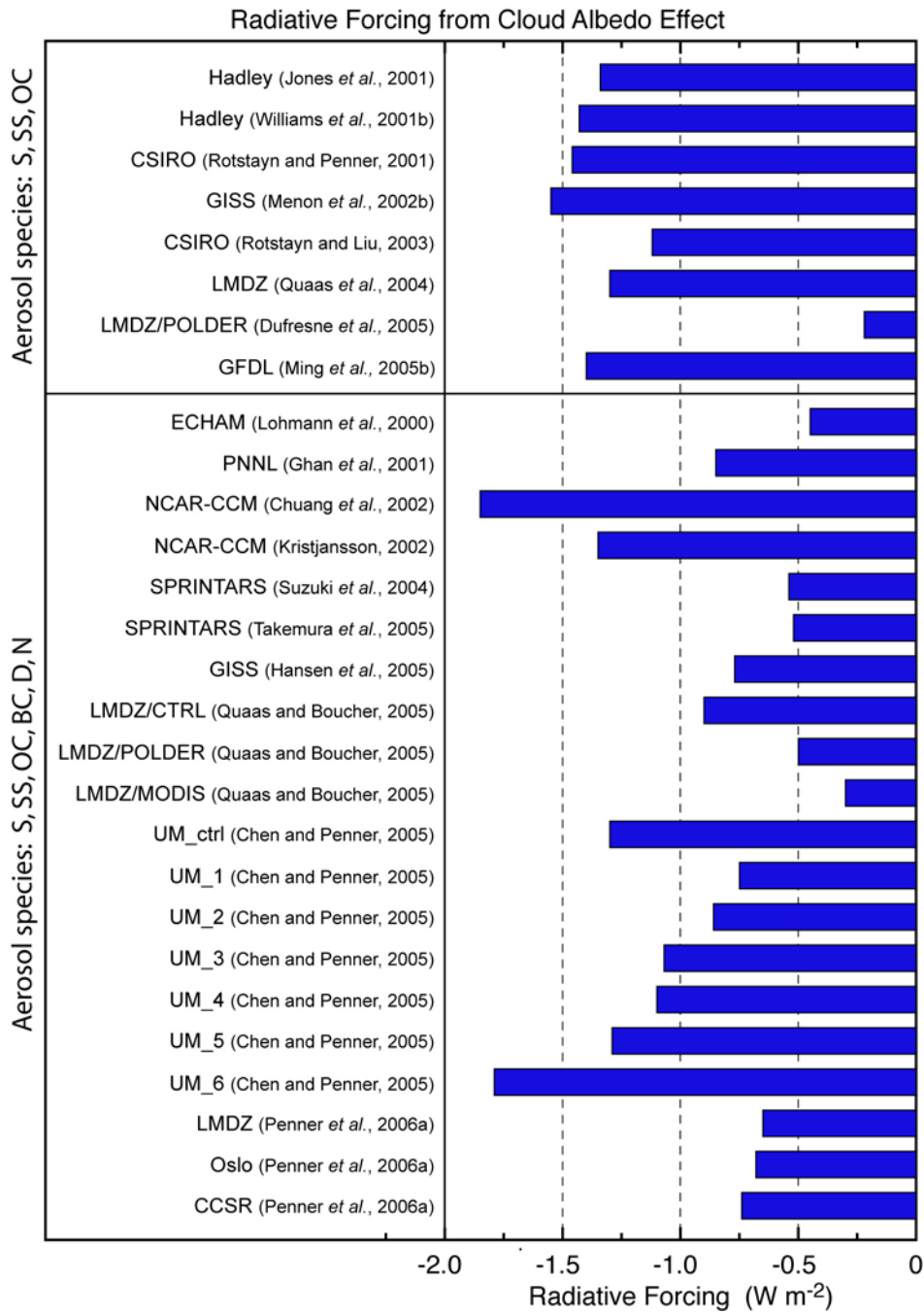
1
2



3
4
5
6
7
8
9

Figure 2.13. Estimates of the direct aerosol RF since the TAR from observational based studies, independent modelling studies, and AEROCOM results with identical aerosol and aerosol precursor emissions. GISS_1 refers to a study employing an internal mixture of aerosol, and GISS_2 to a study employing an external mixture.

1
2



3
4
5
6
7
8
9
10
11
12
13
14

Figure 2.14. Radiative forcing due to the cloud albedo effect, in the context of liquid water clouds, from the global climate models that appear in Table 2.7. The labels next to the bars correspond to the published study; the notes of Table 2.7 explains the species abbreviations listed on the left hand side. Top panel: results correspond to models that consider a limited number of species, primarily anthropogenic sulphate (S). Bottom panel: results correspond to studies that include a variety of aerosol compositions and mixtures; the estimates here cover a larger range than those in the top panel. Chen and Penner (2005) present a sensitivity study changing parameterizations in their model, so that the results can be considered independent and are thus listed separately. Penner et al. (2006a) is an intercomparison study, so the results of the individual models are listed separately.

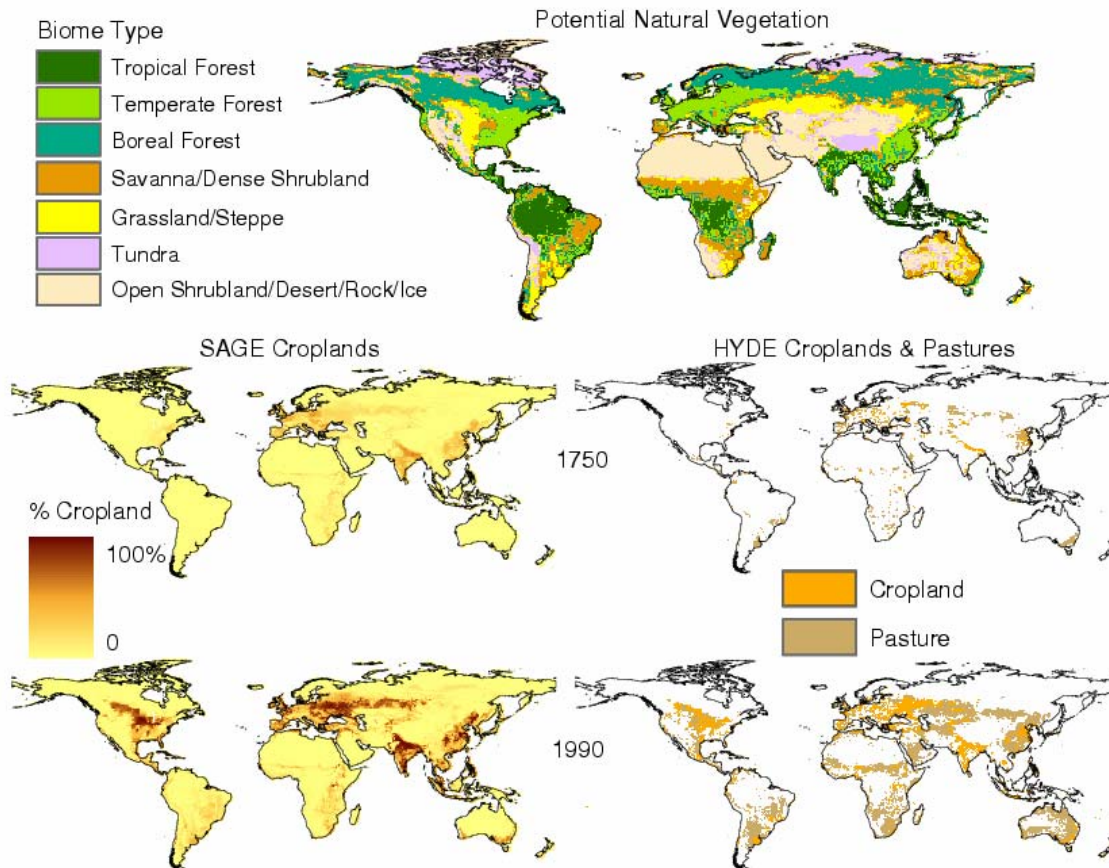
1
23
4
5
6
7
8
9
10
11

Figure 2.15. Anthropogenic modifications of land cover up to 1990. Top panel: Reconstructions of potential natural vegetation (Haxeltine and Prentice, 1996). Lower panels: reconstructions of croplands and pasture at 1750 and 1990. Left-hand column: fractional cover of croplands from SAGE (Centre for Sustainability and the Global Environment, University of Wisconsin; Ramankutty and Foley, 1999), at 0.5° resolution. Right-hand column: reconstructions from the HistorY Database of the Environment (HYDE), RIVM, Netherlands (Klein Goldewijk, 2001), with one land cover classification per 0.5° grid box.

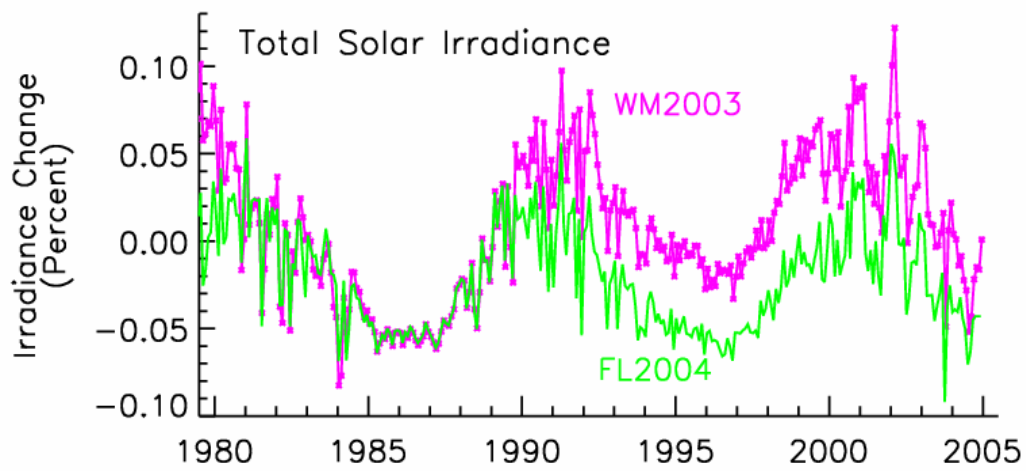
1
23
4
5
6
7

Figure 2.16. Percentage changes in monthly values of the total solar irradiance composites of Willson and Mordvinov (2003) (WM2003, red symbols) and Fröhlich and Lean (2004) (FL2004, green solid line).

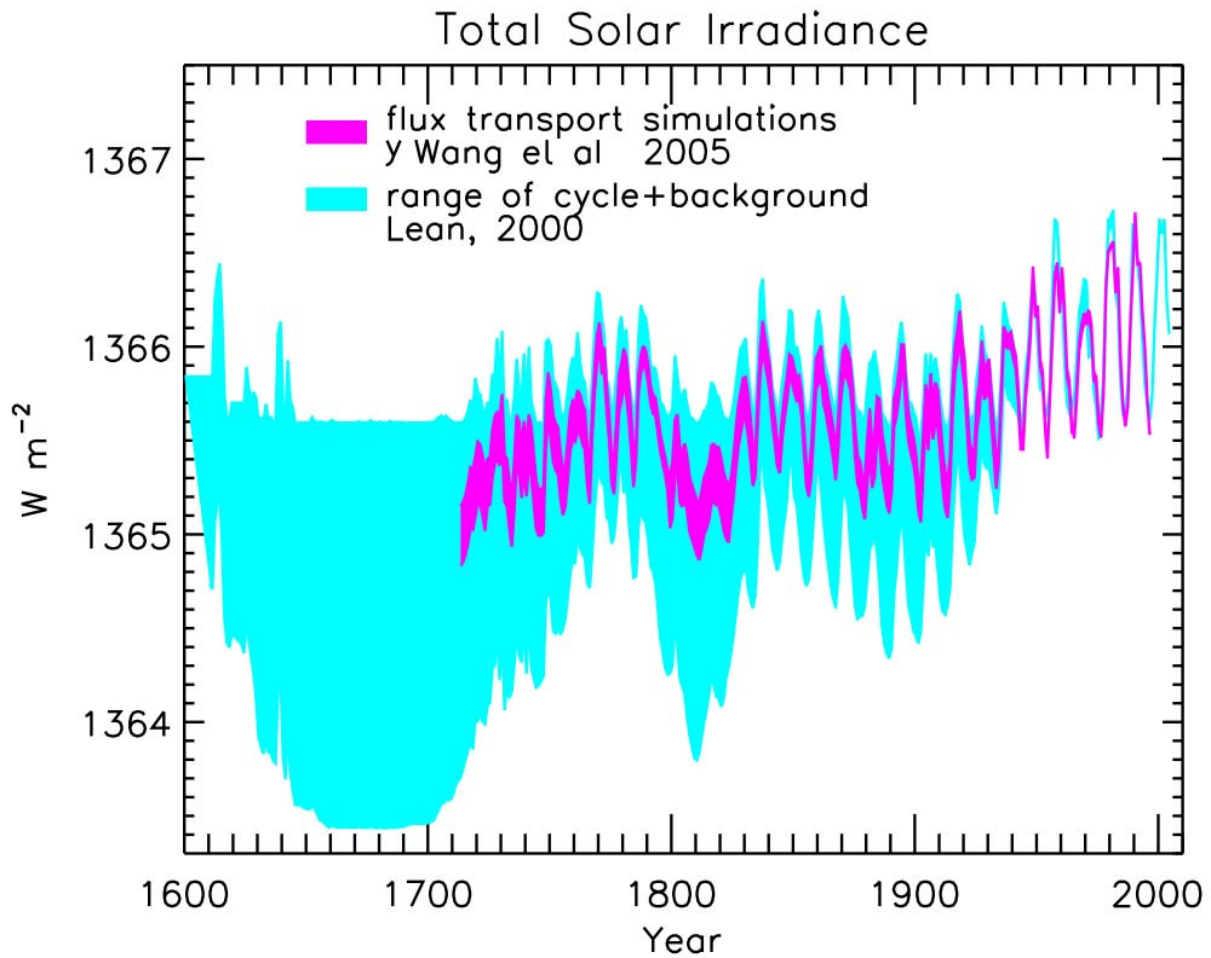
1
23
4
5
6
7
8
9
10
11

Figure 2.17. Reconstructions of the total solar irradiance timeseries starting as early as 1600. The upper envelope of the shaded regions show irradiance variations arising from the 11-year activity cycle. The lower envelope is the total irradiance reconstructed by Lean (2000), in which the long-term trend was inferred from brightness changes in Sun-like stars. In comparison the recent reconstruction of Y. Wang et al. (2005) is based on solar considerations alone, using a flux transport model to simulate the long-term evolution of the closed flux that generates bright faculae.

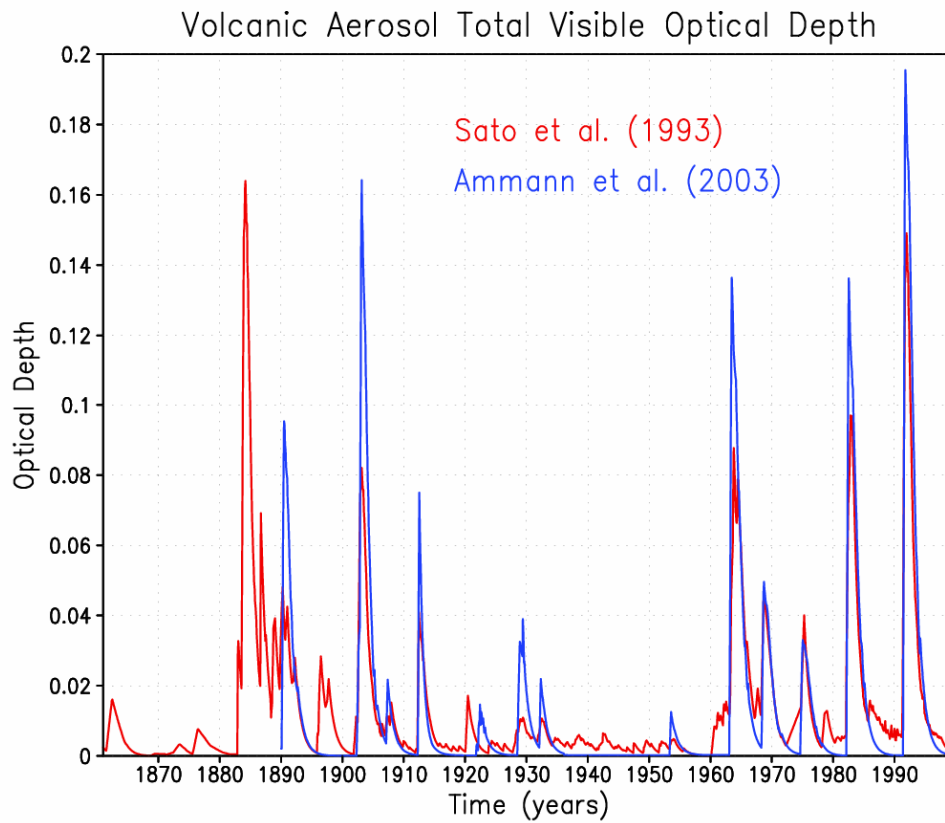
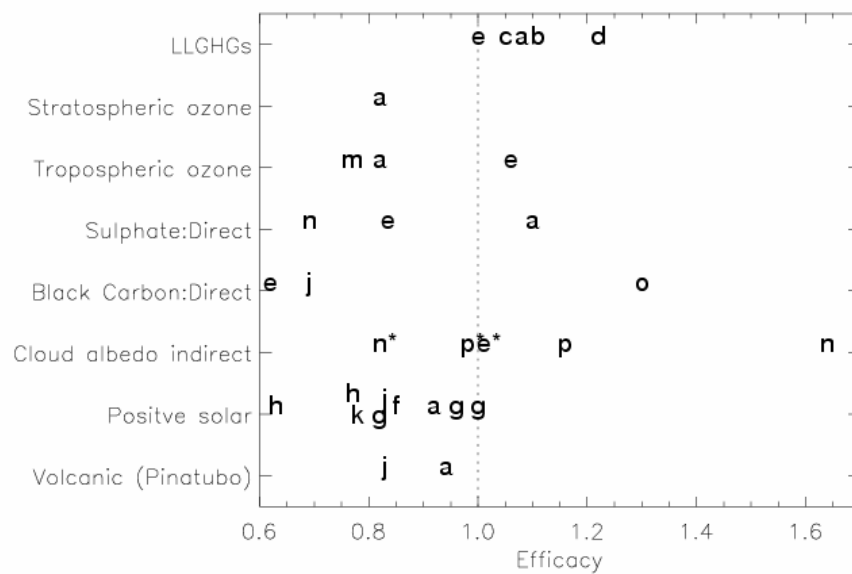
1
23
4
5
6
7
8
9

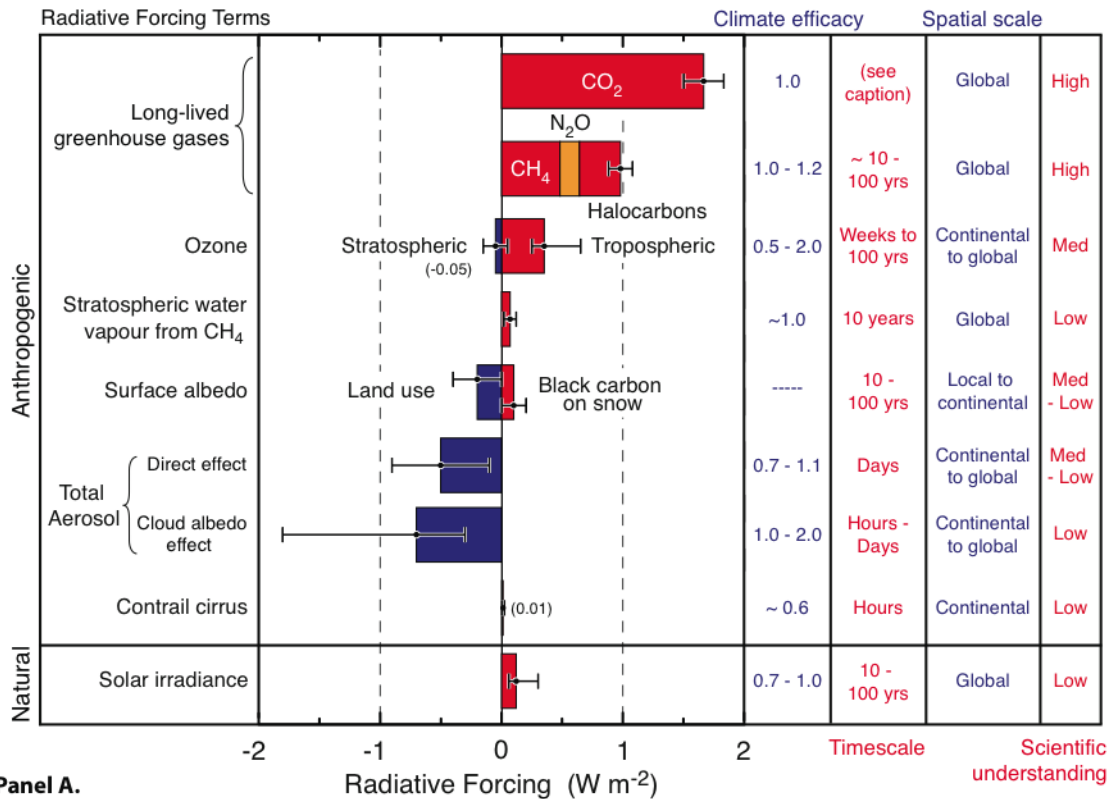
Figure 2.18. Visible (wavelength of 0.55 μm) optical depth estimates of stratospheric sulfate aerosols formed in the aftermath of explosive volcanic eruptions that occurred between 1860 and 2000. Results are shown from two different datasets that have been used in recent climate model integrations. Note that the Ammann et al. (2003) data begins in 1890.

1
23
4

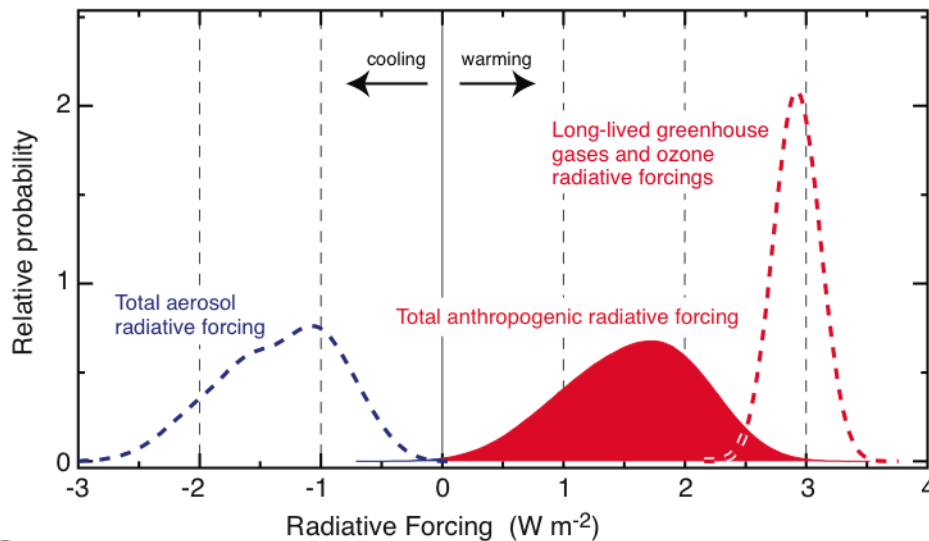
5 **Figure 2.19.** Efficacies as calculated by several GCM models for realistic changes in RF agents. Letters are
6 centred on efficacy value and refer to the literature study that the value is taken from (see text of Section
7 2.8.5 for details and further discussion). In each RF category only one result is taken per model or model-
8 formulation. Cloud-albedo efficacies are evaluated in two ways: the standard letters include cloud-lifetime
9 effects in the efficacy term and the asterixed letters exclude these effects. Studies assessed in the figure are:
10 a) Hansen et al. (2005); b) Wang et al. (1991); c) Wang et al. (1992); d) Govindasamy et al. (2001b); e)
11 Lohmann and Feichter (2005); f) Forster et al. (2000); g) Joshi et al. (2003) (see also Stuber et al., 2001b); h)
12 Gregory et al. (2004); j) Sokolov (2006); k) Cook and Highwood (2004); m) Mickley et al. (2004); n)
13 Rotstayn and Penner (2001); o) Roberts and Jones (2004); p) Williams et al. (2001a).

14

Radiative forcing of climate between 1750 and 2005



Panel A.

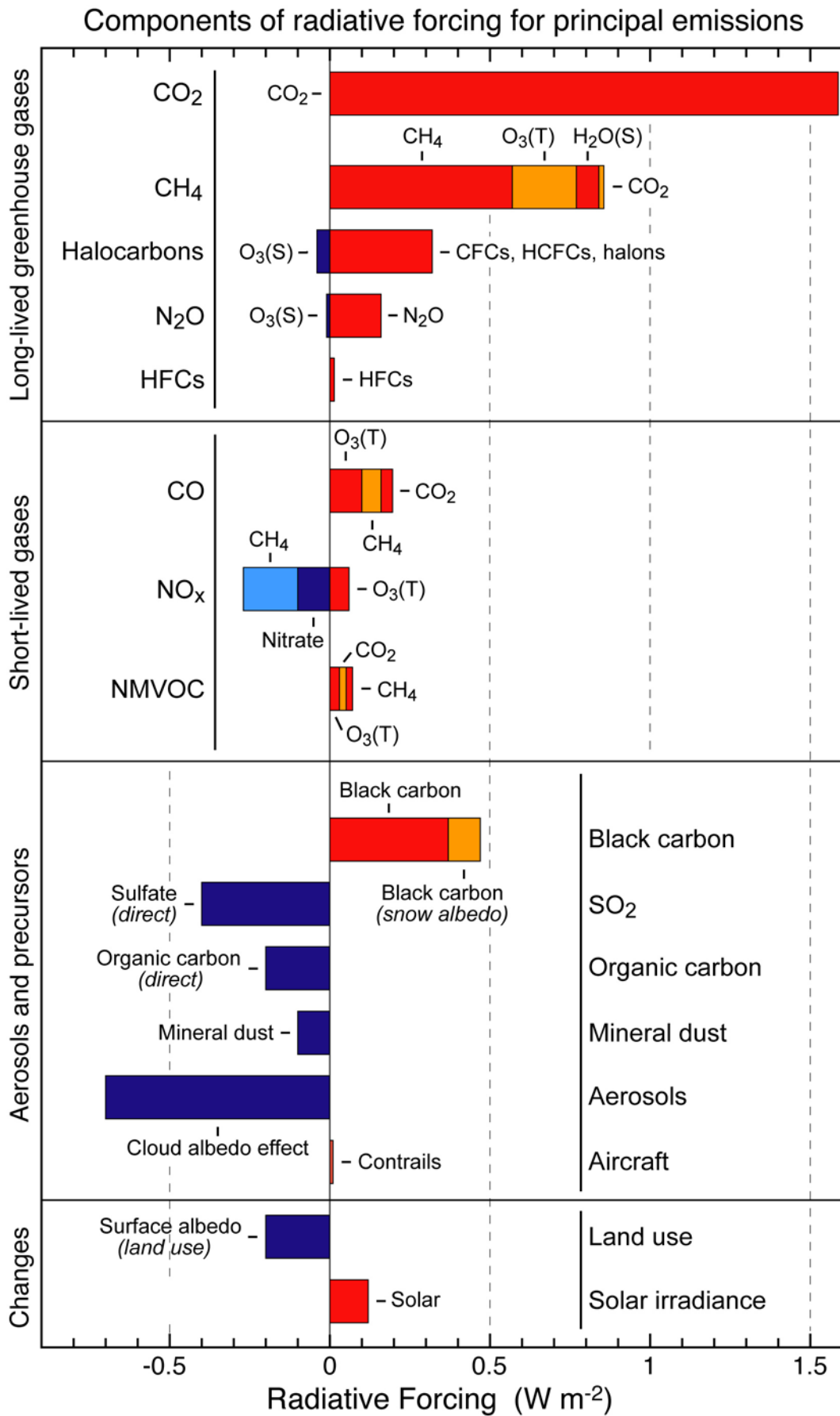


Panel B.

1
2
3
4
5
6
7
8
9
10
11
12
13
14
15
16

Figure 2.20. Panel A: Global mean RFs from the agents and mechanisms discussed in this Chapter, grouped by agent type. Anthropogenic RFs and the natural direct solar RF are shown. The plotted RF values correspond to the bold values in Table 2.12. Columns indicate other characteristics of the RF; efficacies are not used to modify the RFs shown. Timescales represent the length of time that a given RF term would persist in the atmosphere after the associated emissions and changes ceased. No CO₂ timescale is given as its removal from the atmosphere involves a range of processes that can span long timescales, and thus cannot be expressed accurately with a narrow range of lifetime values. The scientific understanding shown for each term is described in Table 2.11. **Panel B.** Probability distribution functions (*PDFs*) from combining anthropogenic RFs in Panel A. Three cases are shown: total of all anthropogenic RF terms (block filled red curve); long-lived GHGs and ozone RFs only (dashed red curve); and aerosol direct and cloud albedo RFs only (dashed blue curve). Surface albedo, contrails and stratospheric water vapour RFs are included in the total curve but not in the others. For all of the contributing forcing agents, the uncertainty is assumed to be

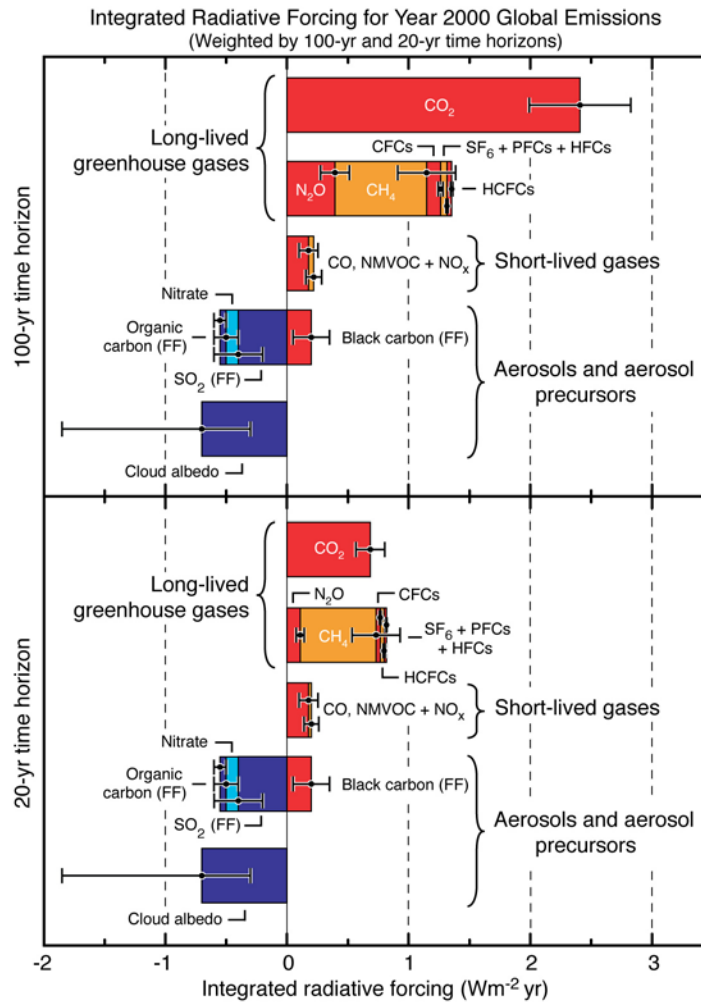
1 represented by a normal distribution (and 90% confidence intervals) with the following exceptions: contrails
2 - a log-normal distribution is assumed to account for the fact that the uncertainty is quoted as a factor of 3;
3 tropospheric ozone and the direct aerosol RF (sulphate, fossil fuel organic and black carbon, biomass
4 burning aerosols) and the cloud albedo RF, discrete values based on Figure 2.9, Table 2.6, and Table 2.7
5 are randomly sampled. Additional normal distributions are included in the direct aerosol effect for nitrate and
6 mineral dust as these are not explicitly accounted for in Table 2.6. A one million point Monte-Carlo
7 simulation is performed to derive the *PDFs* (Boucher and Haywood, 2001). Natural RFs (solar and volcanic)
8 are not included in these three *PDF*. Climate efficacies are not accounted for in forming the *PDFs*.
9



1
2
3
4
5

Figure 2.21. Components of RF for emissions of principal gases, aerosols and aerosol precursors and other changes. Values represent RF in 2005 due to emissions and changes since 1750. The uncertainties are given in the footnotes to Table 2.13.

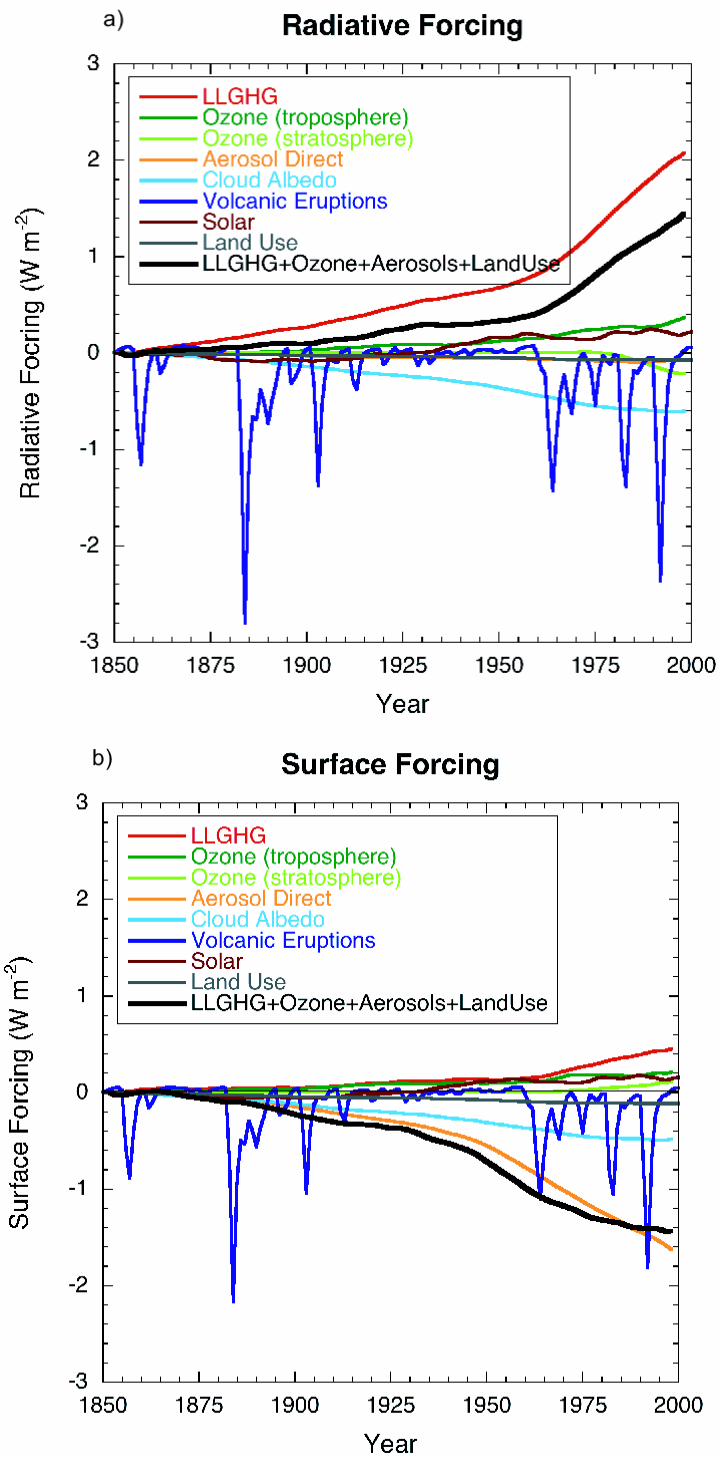
1
2



3
4
5
6
7
8
9
10
11
12

Figure 2.22. Integrated RF over two time horizons (20 and 100 years) of year 2000 emissions. The figure gives an indication of the future climate impact of current emissions. The values for aerosols and aerosol precursors are essentially equal for the two time horizons. It should be noted the RF of short-lived gases and aerosol depend critically on both when and where they are emitted; the values given in the figure apply only to total global annual emissions. For OC and BC, both fossil fuel and biomass burning emissions are included. The uncertainty estimates are based on the uncertainties in emission sources, lifetime and radiative efficiency estimates.

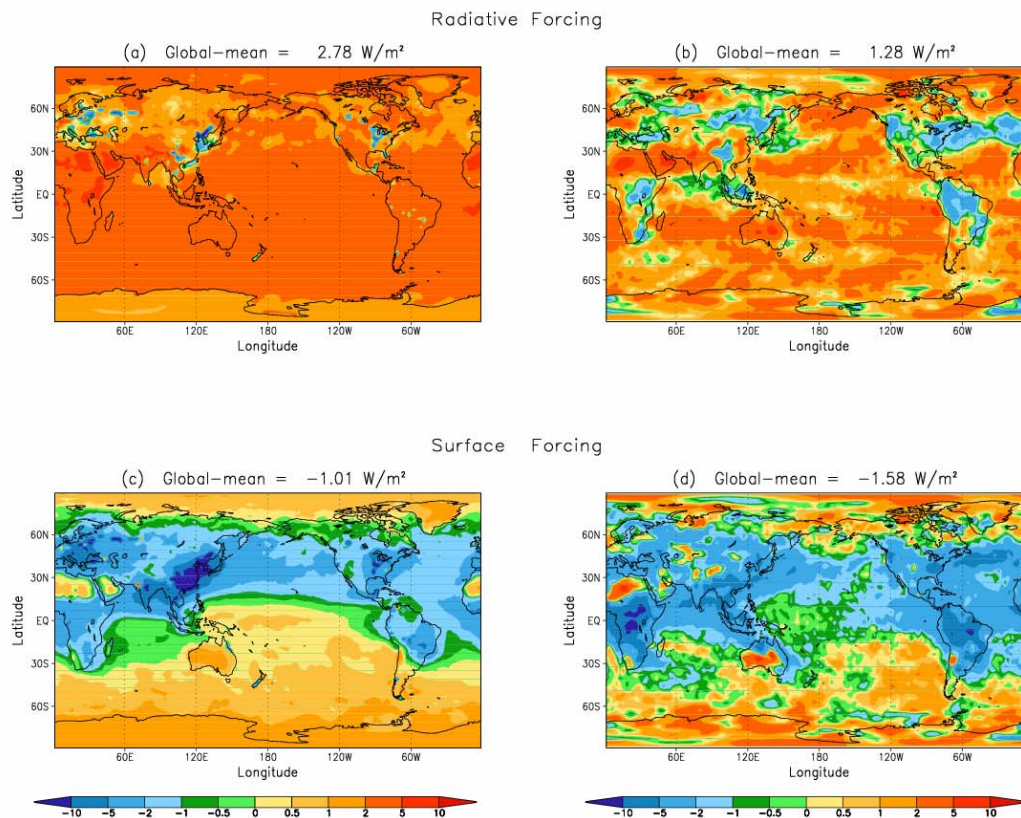
1
2



3

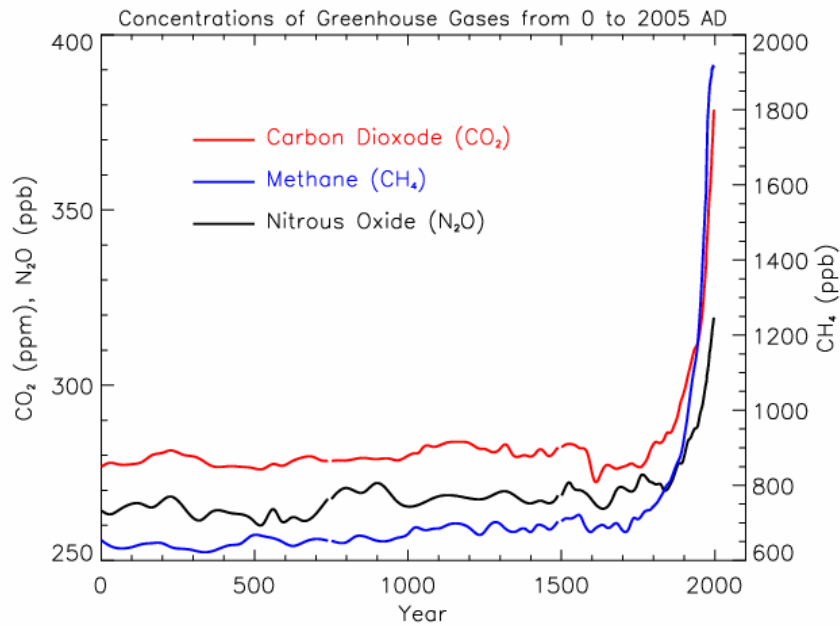
4
5
6
7
8
9
10
11

Figure 2.23. Globally and annually averaged temporal evolution of the instantaneous all-sky RF (top panel) and *surface forcing* (bottom panel) due to various agents, as simulated in the MIROC+SPRINTARS model (Takemura et al., 2005; Nozawa et al., 2005). This is an illustrative example of the forcings as implemented and computed in one of the climate models participating in the IPCC AR4. Note that there could be differences amongst models in the RFs. Most models have roughly similar evolution of the LLGHGs' RF.

1
23
4

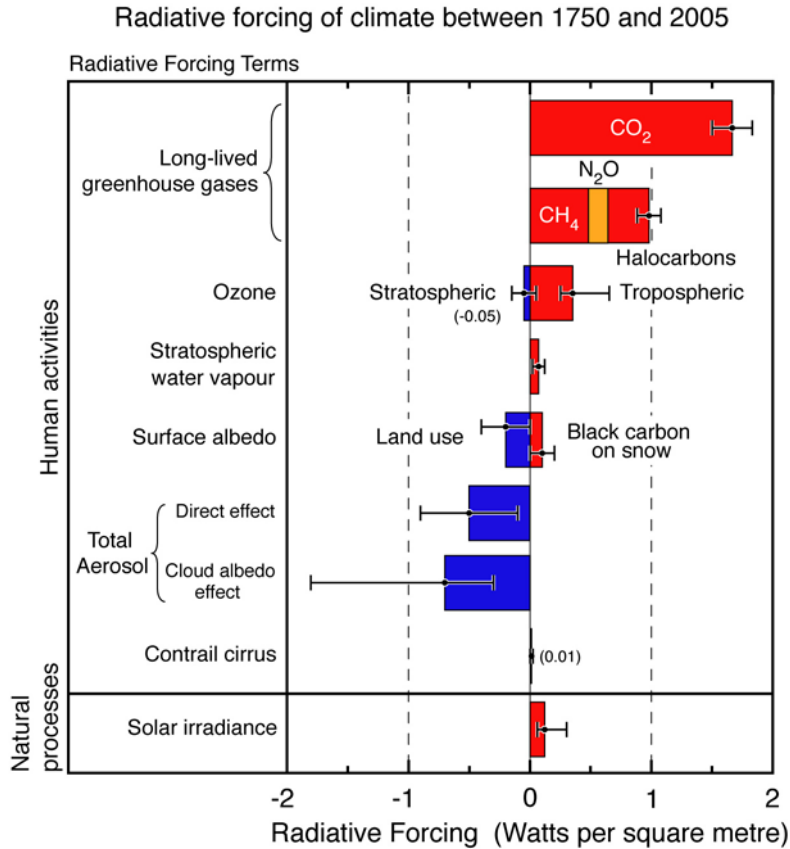
5 **Figure 2.24.** Instantaneous change in the spatial distribution of the net (solar plus longwave) radiative flux
 6 due to natural-plus-anthropogenic forcings between the years 2000 and 1860. Results here are intended to be
 7 illustrative examples of these quantities in two different climate models. (a) and (c) correspond to tropopause
 8 and surface results using the GFDL CM 2.1 model (adapted from Knutson et al., 2006). (b) and (d)
 9 correspond to tropopause and surface results using the MIROC+SPRINTARS model (adapted from Nozawa
 10 et al., 2005 and Takemura et al., 2005). Note that the MIROC+SPRINTARS model takes into account the
 11 aerosol cloud albedo effect while the CM 2.1 model does not.

12
13

1
23
4
5
6
7
8
9
10

FAQ 2.1, Figure 1. Atmospheric concentrations of important long-lived greenhouse gases over the last 2000 years. Increases since about 1750 are attributed to human activities in the industrial era. Concentration units are parts per million (ppm) or parts per billion (ppb) indicating the number of molecules of the greenhouse gas per million or billion air molecules, respectively, in an atmospheric sample. (Data combined and simplified from Chapters 6 and 2 of this report).

1
2



3
4
5
6
7
8
9
10
11
12
13

FAQ 2.1, Figure 2. Summary of the principal components of the radiative forcing of climate change. All these radiative forcings result from one or more factors that affect climate and are associated with human activities or natural processes as discussed in the text. The values represent the forcings in 2005 relative to the start of the industrial era (about 1750). Human activities cause significant changes in long-lived gases, ozone, water vapour, surface albedo, aerosols, and contrails. The only increase in natural forcing of any significance between 1750 and 2005 occurred in solar irradiance. Positive forcings lead to warming of climate and negative forcings lead to a cooling. The thin black line attached to each coloured bar represents the range of uncertainty for the respective value. (Figure adapted from Figure 2.20 of this report.)